第 41 卷 第 3 期
2026 年 6 月

新型炭材料（中英文）
New Carbon Materials

Discontinuous ablation behavior of four-directional dual-matrix C/C composites under dual-pulse solid rocket motors

Wei Lianfeng[1,2,†], Wang Running[1,†], Zhang Jiaping[1,*], Li Kezhi[1], Cui Hong[1,2,*]

(1. *Science and Technology on Thermostructural Composite Materials Laboratory*, *Shaanxi Key Laboratory of Fiber Reinforced Light Composite Materials*, *Northwestern Polytechnical University*, *Xi'an* 710072, *China*;
2. *Xi'an Aerospace Composites Research Institute*, *Xi'an* 710025, *China*)

Abstract: Four-directional dual-matrix C/C composites were fabricated from PAN-based carbon fibers using a combined approach of soft-hard hybrid weaving preform molding, chemical vapor infiltration (CVI) of pyrolytic carbon (PyC), high pressure impregnation and carbonization of pitch-derived carbon. The ablation resistance of the composites was evaluated by testing in a dual-pulse solid rocket motor, and their ablation behavior was investigated. The carbon rods formed by twisting and carbonizing fiber bundles, exhibited a hexagonal cross-section, surrounded by a dense PyC "wall" structure formed during the CVI process. The linear ablation rates of the composites after pulse I and pulse II were 0.068 mm/s and 0.113 mm/s, respectively. A cellular-like PyC layer and nanowire structures were deposited on the surface of the throat convergent section during the post-combustion cooling phase, while cracks and delamination occurred on and within the divergent section. The ablation of C/C composites under these conditions was a complex multi-mechanism process, including ultra-high temperatures, high-speed gas scouring, oxygen-containing thermochemical ablation, and thermal shock. This work elucidates the ablation behaviors of C/C composites under dual-pulse conditions and provides technical guidance and a theoretical basis for designing and fabricating C/C composites for extreme ablation environments.

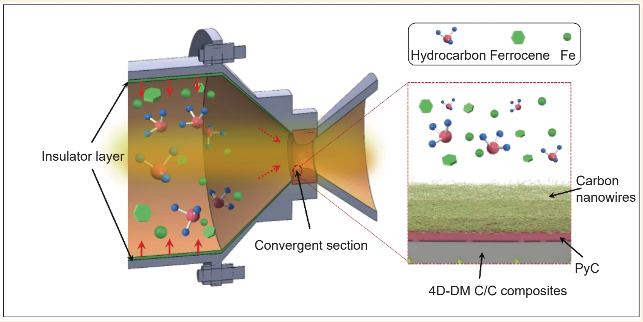

Key words: C/C composites; Ablation; Dual-pulse solid rocket motor; Microstructure evolution; Four-directional dual-matrix

1 Introduction

Carbon fiber-reinforced carbon matrix (C/C) composites are renowned for their excellent thermomechanical properties and ablation resistance at high temperatures, making them widely used in nozzle throats of solid rocket motors[1–2]. During motor operation, the throat lining faces extremely harsh environments characterized by ultra-high temperatures and high-speed gas scouring, inevitably leading to surface ablation[3–6]. Ablation causes mass loss and structural integrity degradation, affecting the normal operation and service life of the entire thermal protection system[7–10]. Thus, the ablation process of C/C composites has become a key research focus in solid rocket motor (SRM) service. Studies have shown that C/C composite ablation involves thermochemical ablation and mechanical ablation[11–13]. Thermochemical ablation refers to material oxidation at high temperatures, while mechanical erosion refers to the spalling of carbon fibers and matrix under gas flow shear stress. Qin et al.[14] developed a multi-scale thermochemical ablation model for multidirectional C/C composites used in SRM, capturing the evolution of ablation morphologies across different scales. Li et al.[15] investigated the ablation behavior of various fiber-reinforced C/C

Received: August 18, 2025
Revised: December 14, 2025
Accepted: December 15, 2025

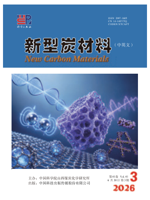

composites under small SRM test conditions. Wang et al.[16] studied the influence of specific overload conditions in solid rocket motors on the throat ablation rate of C/C composites.

To meet the higher reliability requirements of SRM, C/C composites need improvements in both preform structure and matrix. In preform optimization, different structures like 2D[17], 3D[18–19] and 4D[20–21] have been explored, with 4D C/C composites showing greater potential[22]. Zahid et al.[23] found that 4D C/C composites exhibit superior thermal shock resistance compared to their 2D counterparts. For matrix modification, ultra-high temperature ceramics (UHTCs)-modified C/C composites can enhance ablation resistance within a certain temperature range[5,24–26], but inherent issues like low service temperature and thermal expansion mismatch limit their application in extreme SRM environments. Pyrolytic carbon (PyC) deposited by chemical vapor infiltration (CVI) can improve ablation resistance[27], but the CVI limitations make it difficult to achieve high density[28]. A pitch-derived carbon (PDC) matrix can be densified under higher pressure[29], enabling the production of higher density materials. Therefore, combining 4D preforms, PyC, and PDC matrix holds promise for fabricating C/C composites with high density and good ablation resistance.

At present, the research on ablation properties of 4D C/C composites includes plasma ablation[30], oxy-acetylene ablation[31], oxygen kerosene ablation[32], etc. However, there are only a few studies on its performance in discontinuous motor simulation tests[2,15]. For dual-pulse SRM, which have attracted extensive attention due to their high flight mobility and real-time energy distribution[33–34], the nozzle throat components face discontinuous ablation from two or more pulses. The ablation interval exposes the material to rapid heating, cooling, and re-heating, leading to drastic temperature fluctuations and discontinuous thermal, mechanical, and ablation coupling—significantly different from the single continuous ablation in traditional motors. Currently, studies on discontinuous ablation behavior of C/C composites are limited. In order to make up for this gap, we employed a dual-pulse motor test to simulate a more realistic, step-by-step ablation process.

In this work, we leveraged the advantages of 4D preforms, PyC, and PDC matrices to prepare four-directional dual-matrix C/C composites through multi-directional soft-hard hybrid weaving, CVI, and high pressure impregnation and carbonization (HPIC). The microstructure evolution during preparation was analyzed, and the ablation resistance was evaluated via dual-pulse motor tests. The ablation behavior and mechanism were obtained by analyzing the post-test microstructure, providing guidance for the preparation and reliability design of C/C composites for dual-pulse motors.

2 Experiments

2.1 Material preparation

The C/C composites were fabricated from polyacrylonitrile-based carbon fibers and dual carbon matrices. Carbon fiber bundles (T300, 3K, Jilin Carbon Co., China) were merged into larger bundles using a twisting machine. The loose fiber bundle can be bonded by impregnating phenolic resin, and formed into carbon rods by a wire drawing machine. The carbon bundles and rods (35%–40%) were woven into a 3D four-directional preform (Fig. 1). The carbon rods have a diameter of 1.5 mm with a spacing of 4 mm. The fiber bundles measure 2.0 mm in width and 0.6 mm in thickness, arranged along the U, X and W axes in the same plane, stacked sequentially, with carbon rods aligned along the Z-axis perpendicular to the bundles. Each carbon rod can be regarded as a unit cell, as indicated by the yellow dashed area.

The 4D preform (Φ130 mm×120 mm) with a density of 0.70–0.80 g/cm^3 underwent high-temperature pretreatment (HTP) at 2100 °C, followed by multi-cycle CVI densification using C_3H_6 and N_2 at 900–1000 °C and pressure of 4–8 kPa. The content of the resin derived carbon after pyrolysis is very low, so it is not considered as a matrix. Pitch impregnation (PI) and hot isostatic pressing carbonization (HIPC) were then employed for further densification. Several

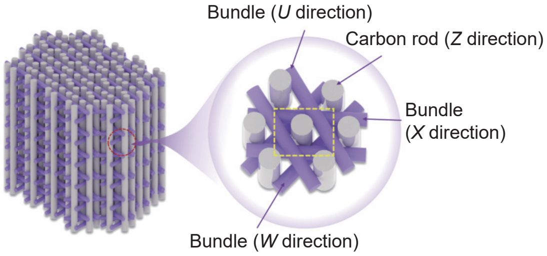

Fig. 1 Schematic model of 4D preform

high-temperature treatments (HTT) at 2500 °C were conducted to open pores for subsequent impregnation-carbonization cycles. Details about these processes are provided in ref [35]. The final density of the C/C samples is approximately 1.95 g/cm^3. The mass fractions of PyC and PDC are both 25%–30%. The preparation process flowchart of 4D-DM C/C composites is shown in Fig. 2.

2.2 Testing and characterization

The as-prepared 4D-DM C/C composite blanks (Φ120 mm×115 mm) were machined into throat components, which were assembled into the nozzle of a dual-pulse solid rocket motor (DPSRM) for ablation testing (Fig. 3). The test system mainly comprised pulse I, a pulse isolation device, pulse II, and a nozzle. Hydroxyl-terminated polybutadiene (HTPB)/ammonium perchlorate (AP) propellant was used. Pulse I operated for 16.1 s, pulse II for 19.8 s, with a 21 s interval between pulses.

The throat diameter was measured by a micrometer before the test, and in the process of testing it was calculated using the equilibrium pressure formula based on pressure changes during propellant combustion[15]:

$$d_\mathrm{t} = \sqrt{\frac{4\rho a c A_\mathrm{b}}{\pi p^{1-n}}} \tag{1}$$

where d_t is the throat diameter, ρ is the propellant density, a is the combustion rate coefficient, c is the characteristic velocity, A_b is the combustion surface area, p is the chamber pressure, and n is the pressure index.

The linear ablation rate was calculated as:

$$R_\mathrm{l} = \frac{d_0 - d_\mathrm{i}}{2t} \tag{2}$$

where R_l is the linear ablation rate, t is ablation time, and d_0, d_i are throat diameters before and after ablation, respectively.

The engine pressure is mainly obtained by measuring the pressure fluctuation in the chamber through the built-in pressure sensor. Due to high impulse, elevated temperatures, and severe disturbance of the plume conventional experimental techniques struggle to measure the surface temperature of the samples. The real-time temperature of the back wall of the specimen is measured by a thermocouple fixed at its center. Based on this, a computational fluid dynamics method was employed to simulate the temperature of the specimen. Similar approaches can be referenced in

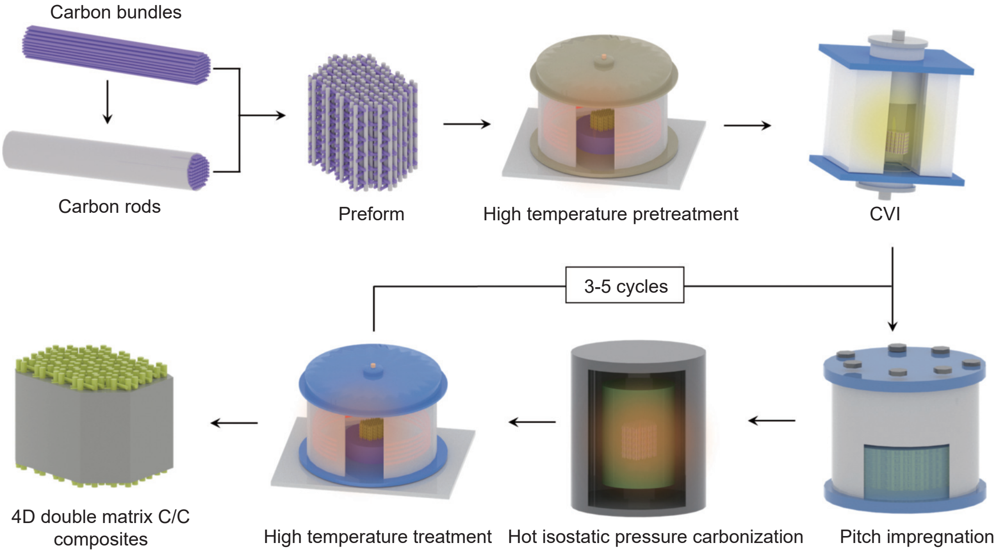

Fig. 2 Fabrication procedure for multidirectional dual-matrix C/C composite

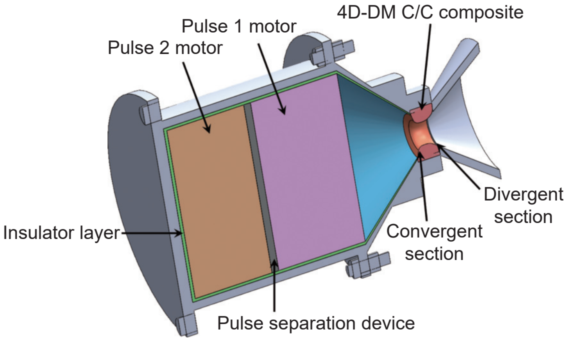

Fig. 3 Schematic diagram of the double-pulse SRM test

the literature[36].

The density was determined by the Archimedes' method. Microstructures were characterized using an optical microscope (OM, Leica DMLP, Germany), a polarizing microscope (PLM, Leica DMLP), and scanning electron microscope (SEM, JSM-7800F, JEOL, Japan) with energy-dispersive spectroscope (EDS, Oxford-INCA, UK) before and after ablation. PLM and OM samples were immersed in epoxy resin, polished with silicon carbide, and diamond powder-coated polishing cloths. Internal defects of ablated materials were detected using an X-ray real-time imaging detection system (X–RTIDS, SZT-800, Lanzhou Sanlei Testing Technology, China). Raman spectroscopy was used to analyze the microstructure and chemical composition of the composites with laser wavelength of 514 nm.

3 Results and discussion

3.1 Microstructure of as-prepared composites

The microstructure of the as-prepared 4D-DM C/C composites is shown in Fig. 4. Fig. 4a shows an OM image of the yellow-line area in Fig. 1, revealing that carbon rods are roughly hexagonal (red-line area), with 2D carbon fiber bundles forming triangular regions (green-line area). Fig. 4(b-d) show the SEM images of cross-section of sample, indicating thick PyC layers deposited at carbon rod edges, demonstrating that PyC not only fills gaps between carbon fibers in rods and bundles but also forms a thick layer outside during CVI (Fig. 4c). PyC exhibits good interfacial bonding with the fibers. Additionally, the PDC matrix mainly exists in the triangular regions between carbon rods and fiber bundles, and it forms a layered structure due to multiple impregnation and pyrolysis cycles during preparation (Fig. 4d). Some cracks can be observed between PyC and PDC. Raman spectra of carbon fiber, PyC, and PDC reveal that the I_D/I_G ratio indicates graphitization degree (Fig. 4e). Results showed that PyC exhibited the lowest I_D/I_G value, indicating the highest graphitization degree, i.e., the highest degree of carbon ordering.

Based on the analysis, 4D-DM C/C composites consist of 5 constituents: single carbon fibers, carbon

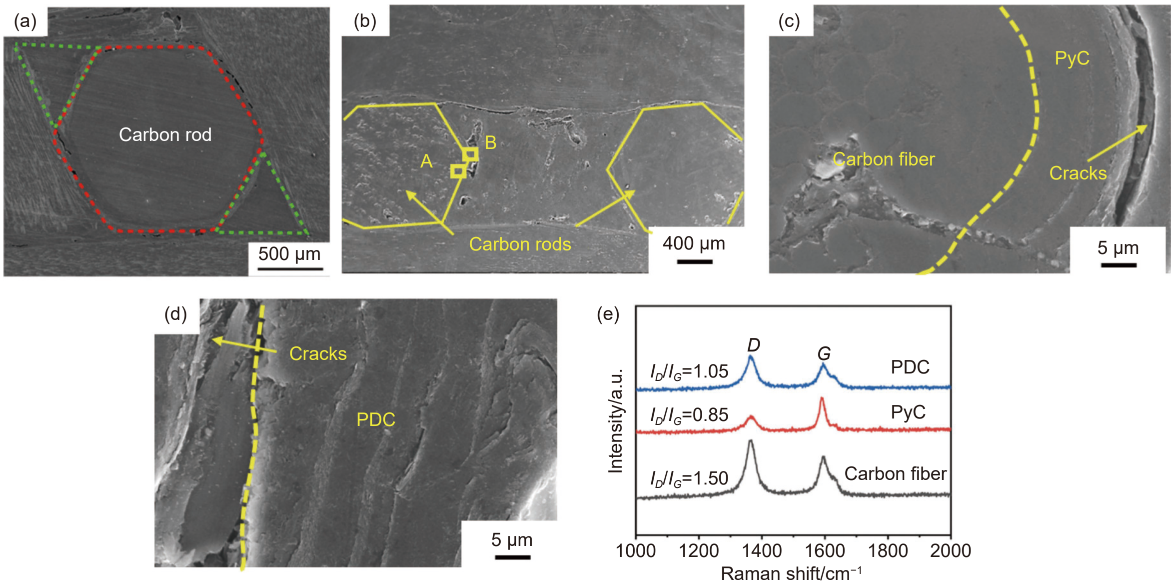

Fig. 4 Microstructure and Raman spectra of 4D-DM C/C composites: (a) OM image. (b) Low magnification SEM image. (c) Region A. (d) Region B. (e) Raman spectra

bundles, carbon rods, PyC matrix and PDC matrix. The microstructure evolution during preparation is schematically shown in Fig. 5. HTP leads to the carbonization of internal resin and the creation of small open pores, which subsequently loosen the carbon rods. Unconstrained by resin, the loose rods are constrained and extruded by the U, X and W carbon bundles (oriented at 60°) into a hexagonal shape (Fig. 5b). The CVI process initially densifies the pores within the carbon rods and bundles with PyC. Following this, as CVI progresses outwards, C_3H_6 deposition on the rod/bundle surfaces forms a thick PyC layer after gap infiltration (Fig. 5c). During PI and HPIC, this layer serves as a "wall", confining the PDC matrix to the inter-rod and inter-bundle gaps instead of the rod interiors (Fig. 5d). Multiple interfaces are thus generated (e.g., PyC/fiber, PyC/bundle, PyC/rod, and PyC/PDC), which are critical for the subsequent ablation process.

3.2 Ablation resistance

Fig. 6a presents the combustion chamber pressure profile during the operation of a dual-pulse motor. As shown, the chamber pressure rises rapidly upon ignition of pulse I, followed by a sharp decline after the termination of pulse I operation. Post-pulse interval, upon ignition of pulse II, the pressure exhibits another rapid increase, with the average pressure of pulse II being notably higher than that of pulse I. Specifically, both pressure curves decrease as ablation time extends, indicating the diameter changes of throats by ablation. Based on the motor parameter changes during ablation, the throat diameter variation with ablation time was calculated using formula (1) (Fig. 6b). The throat diameter increases gradually during both pulse I and pulse Ⅱ, with no significant change during the interval. The linear ablation rates for pulse I and pulse Ⅱ were calculated using formula (2). The ablation rate after pulse Ⅱ is 0.113 mm/s, which is higher than pulse I (0.068 mm/s), the inner diameter increases, indicating that the combustion rate is higher and can cause higher mechanical ablation. During the ignition of the pulse I and pulse II, the curve of throat surface temperature change can be measured by sensors, as shown in Fig. 6c. Surface temperature rapidly rises to 2842 °C for pulse I, and during pulse II, it increases from 2498 °C to as high as 3085 °C. The heating rate initially accelerates and then slows as ablation time extends. Owing to variations in pressure, gas flow velocity, and temperature, the degree of ablation differs between the convergent and divergent sections. For convergent section, the cross-sectional area decreases towards the throat. According to mass conservation, the gas flow velocity increases, while the static pressure and temperature are relatively high and stable before reaching the throat. This region is thus dominated by high heat flux, high pressure, and intense mechanical scouring. Different from convergent section, the cross-sectional area of divergent section expands. This leads to a further rapid increase in gas velocity and a corresponding sharp decrease in static pressure and temperature. This region, therefore, experiences the highest shear stress from the high-velocity flow and a different regime of thermochemical reactions due to the lower

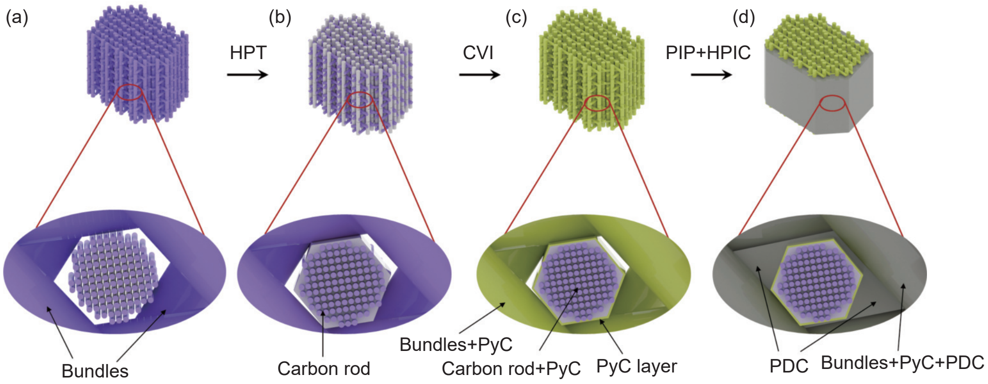

Fig. 5 Schematic of microstructure evolution during fabrication of 4D-DM C/C composites

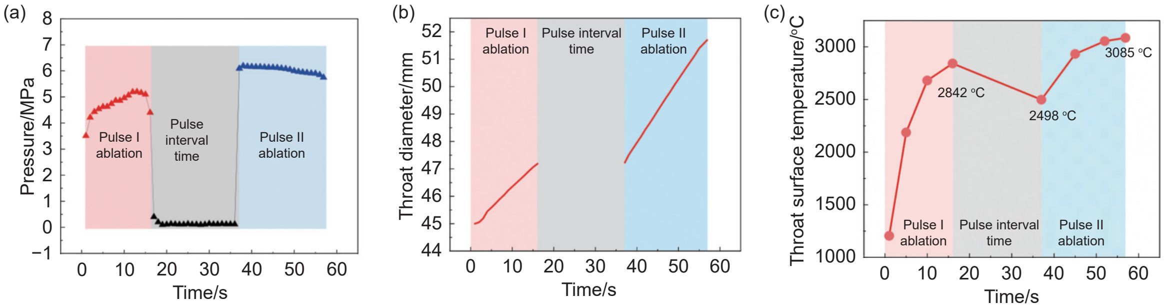

Fig. 6 (a) Pressure, (b) throat diameter variation and (c) throat surface temperature during the ablation process

pressure. Analysis of the ablation microstructure of these regions is discussed in the next section.

3.3 Microscopic morphology analysis

3.3.1 Convergent section

The post-ablation microscopic morphology of the convergent section is shown in Fig. 7. The surface is rough, with convex features around carbon rods/bundles forming valley-like structures and flocculent protrusions (Fig. 7a). Analysis of carbon rods reveals no typical "bamboo shoot tip" structures of carbon fibers on relatively flat surfaces, but a layer of cellular protrusions adheres to the surface (Fig. 7b). Dense cellular coatings form on flat areas (Fig. 7c), which are confirmed to be carbon by EDS. A high-magnification SEM image of the coating cross-section (Fig. 7d) shows distinct cellular protrusions with a thickness of ~ 10 μm. PLM image (Fig. 7e) indicates obvious extinction, suggesting the coating is PyC. Further magnification of the flocculent structures (Fig. 7f) reveals dendritic PyC and nanowire structures. EDS analysis of the nanowire region (yellow dashed area) confirms that they consist of C and trace Fe, which may be generated by iron-catalyzed reactions.

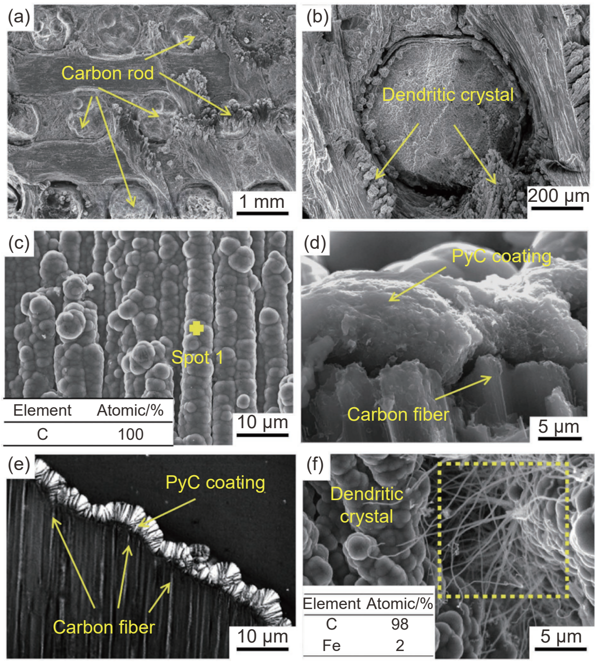

Fig. 7 Micro-morphology of 4D-DM C/C composites after ablation: (a) Low-magnification SEM image. (b) Carbon rods. (c) Cellular coating. (d) High-magnification SEM image of ablation cross-section. (e) Cross-section of PLM image. (f) SEM image and EDS analysis of nanowires

In the structural composition of a SRM combustion chamber, an insulation layer (Fig. 3) between the propellant and the engine casing for thermal protection primarily consists of rubber-based materials, such as ethylene propylene diene monomer (EPDM)[37]. In this work, EPDM was also used for manufacturing the insulation layer. It needs to last several minutes for the combustor to lower the temperature after all the propellant has been consumed. During cooling, the EPDM insulation layer near the propellant undergoes a pyrolytic reaction at high temperature, releasing hydrocarbon gases such as butene, pentene and benzene[38]. As a result of the pressure difference between the inside and outside of the combustor, hydrocarbon gases flow to the nozzle. Under high-temperature conditions, they undergo pyrolysis based on CVD theory and deposit onto the ablation surface. The main reaction is described as follows:

$$C_xH_y(g)\rightarrow C(s)+H_2(g) \qquad (3)$$

Additionally, due to the flow direction, most of the deposition occurred in the convergent section and much less deposition occurred in the divergent section where the temperature was also much lower than that in the convergent section. During pulse II, the deposited EPDM-PyC layer could avoid further mechanical damage to the fibers and matrix, but the gas flow could not be completely isolated by the coating of deposits because of the holes; consequently, the oxidation of the fibers still continued.

On the other hand, ferrocene is widely used in the propellant of SRM as a burning-rate (BR) catalyst[39], which was also employed in the present test device. During motor manufacturing and storage, there is a possibility that ferrocene may migrate from the propellant into the insulation layer[40]. According to a thermal decomposition study of ferrocene[41−42], gaseous ferrocene decomposes spontaneously to form metallic iron at temperatures above ~770 K, according to the following reaction:

$$(C_5H_5)_2Fe \rightarrow Fe+H_2+CH_4+C_5H_6+\cdots \tag{4}$$

After the propellant was consumed, the combustor remained at a high temperature. The ferrocene in the insulation layer was then gasified and decomposed, producing Fe. This Fe was transported through the nozzle along with the gases generated from the decomposition of the insulation materials. As the hydrocarbon gas provided the carbon source and Fe acted as catalytic particles, carbon nanowires were synthesized at high temperature[43−44] (Fig. 8).

The migration of ferrocene in SRM propellants significantly increases the concentration gradient at the propellant-insulation layer interface, leading to combustion rate non-uniformity and fluctuations in internal ballistic parameters[40]. Additionally, this migration process accelerates debonding failure at the interface between the thermal insulation layer and propellant, thereby increasing the risk of motor structural failure[45]. However, as the propellant is permanently sealed within the casing after SRM manufacturing, direct detection of ferrocene migration in the propellant remains challenging at present. The presence of carbon nanowires in the surface of the ablated throat sample can be analyzed to provide a reference for determining the migration of ferrocene.

3.3.2 Divergent section

Fig. 9 shows the post-ablation morphology of the divergent section. Unlike the convergence section, no PyC deposition is observed on the surface, and the microstructure of carbon rods, fibers, PyC and PDC matrices has undergone significant changes. The original PyC layer around carbon rods transforms into a thin-walled circular shell with obvious gully-like gaps on both sides, and internal fibers become loose. Microanalysis of the triangular region between carbon rods and fiber bundles (Fig. 9b) reveals large gaps, with the external matrix carbon ablated, exposing cross-lap structures and increasing surface roughness. The pre-existing microcracks from processing and the cracks formed during ablation significantly affect the ablation morphology (Fig. 4(c, d)). These cracks provide direct channels for the inward diffusion of high-temperature oxidizing species and the outward erosion by the high-speed flame flow. This synergistic effect accelerates the ablation process. After ablation, most PDC in the triangular region is consumed, and the surface reveals a tiered structure: the PyC

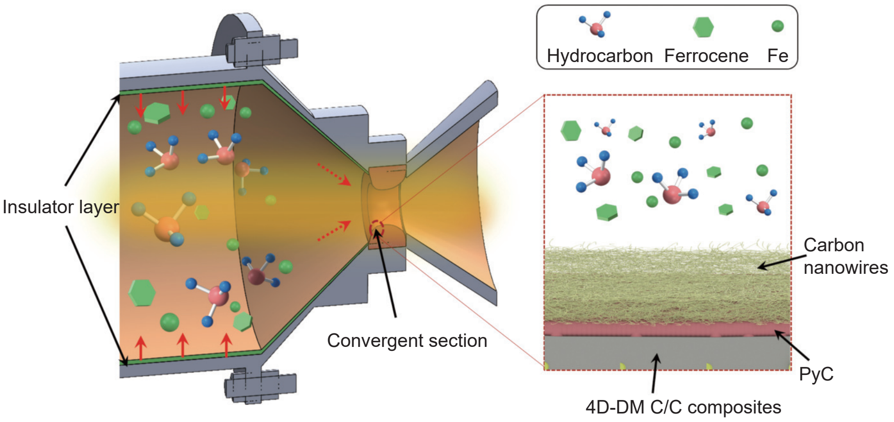

Fig. 8 Schematic diagram of the formation mechanisms of carbon nanowires and PyC coating during ablation

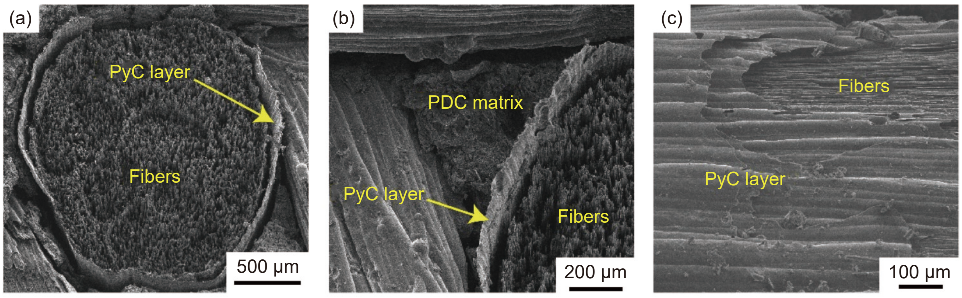

Fig. 9 Surface micro-morphology of material after ablation: (a) Carbon rod. (b) Rod-fiber bundle intersection. (c) Carbon fiber bundle

layers around the carbon rods are the most prominent, followed by the internal fibers, and finally the recessed PDC matrix. This height difference corresponds to the materials' ablation resistance. The ablation resistance order is: PyC shell layer>carbon fiber>PyC matrix>PDC matrix.

Fig. 9c shows the ablation morphology of carbon fiber bundles perpendicular to carbon rods, where external PyC layers are ablated into multi-layered shell structures. Interfaces within PyC layers form gaps after ablation, exposing internal fibers. Fig. 10 shows the microstructural comparison of the PDC matrix before and after ablation. Before ablation, it exhibits an irregular lamellar structure with tight bonding (Fig. 10a). Microstructural analysis of the ablated matrix reveals a loose layered structure (Fig. 10b), resulting from preferential oxidation at the interfaces between two successive PDC layers.

Furthermore, the distinct ablation morphologies of PyC and PDC correlate with their structures and properties. PyC, characterized by a dense structure and high graphitization, exhibits strong fiber bonding. This structure confers excellent resistance to mechanical abrasion and delays oxidation processes. In contrast, PDC is distributed within large, unreinforced pores, making it prone to microcracking. Without fiber reinforcement, this brittle matrix is highly susceptible to fragmentation and delamination by flame flow, ultimately forming grooves and an uneven surface. As shown in Fig. 11, voids exist between the fiber bundles, with some fibers fractured and poor regularity in fiber shape. The main reasons may be as follows: one is that fibers bind poorly with matrix, making the fiber-matrix interfaces and gaps prone to becoming invasion sites for oxidizing gases[46]; and the other is due to the increase in pressure and temperature, as well as the thermal shock effect induced by discontinuous ablation, this renders the matrix and fiber bundles susceptible to fracture and spallation under the scouring of high-velocity gas flow. Fig. 12 shows OM images of the ablated cross-section. Figs. 12(a, b) depict the PyC layer outside carbon fiber bundles and the bulk PDC matrix, respectively. Minor cracks form within both PyC and PDC matrices, accompanied by large-scale spalling near the ablation surface. Fig. 12c shows that carbon fibers transform from circular to irregular shapes after ablation, with many fibers adhering to the material surface and the surrounding matrix becoming loose.

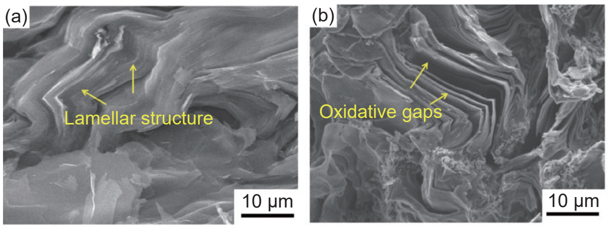

Fig. 10 Microstructure of PDC matrix: (a) before and (b) after ablation

From Fig. 11 and 12, the ablation process of 4D-DM C/C composites under dual-pulse conditions is not only a surface recession but also an internal structure relaxation. To observe the internal morphology, the specimen was cut to a depth of 10 mm along the thickness direction, and the cross-section was pol-

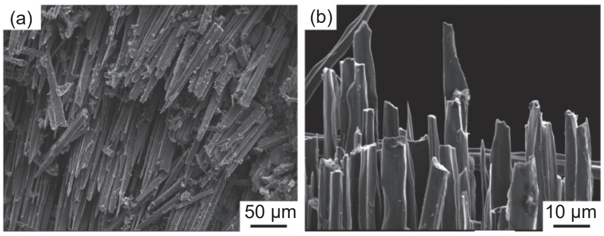

Fig. 11 Microstructure of carbon fibers after ablation

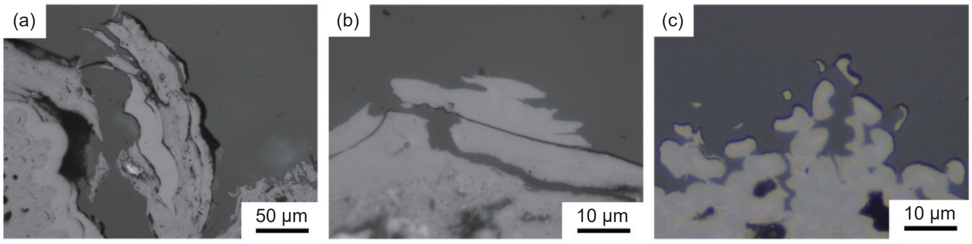

Fig. 12 Optical micrographs of the ablated specimen cross-section: (a) PyC layer. (b) PDC matrix. (c) Carbon fibers

ished for optical microscopy (Fig. 13). Numerous pores and gaps are visible within carbon rods (Fig. 13b), and cracks form between internal fibers (Fig. 13c), indicating that ablation increases internal defects. The double pulse ablation exhibits a superposition effect, which further exacerbates internal defects. The first pulse ablation already induces surface ablation recession, while forming initial microcracks and pores inside the composites. During pulse II, high temperature gas flow can more easily penetrate into the interior through the channels at the ablated surface. The combined effect of the surface-to-interior temperature gradient and the gas flow scouring generates significant internal stress. This stress concentrates at pre-existing microstructural defects, such as microcrack tips and pore edges, driving their propagation. This mechanism results in the expansion of internal pores, an increase in crack, and the formation of gaps between fiber bundles due to matrix loss, leading to overall structural relaxation.

Moreover, the post-ablation density was measured, yielding a bulk average density of 1.86 g/cm^3, presenting a 4.61% decrease from the pre-ablation value (1.95 g/cm^3). This measured decrease in bulk density quantitatively reflects the overall material loss and the formation of voids and cracks throughout the sample. Ablation in a DPSRM can be regarded as an ultra-high-temperature treatment. On one hand, partial components within the material vaporize at temperatures exceeding 3000 K. On the other hand, high-concentration gases from the combustion chamber enter the material through pores under high pressure, promoting matrix oxidation and thereby accelerating internal mass loss. Two random segments of the ablated 4D-DM C/C composite throat liner were subjected to axial detection using an X-ray real-time imaging system (Fig. 14). The results show varying degrees of through-thickness delamination, further confirming that the discontinuous ablation process in dual-pulse motors significantly affects the internal microstructure.

Based on the above microstructural analysis, different microstructures in 4D-DM C/C composites exhibit distinct evolution processes and ablation sensitivities under dual-pulse conditions. For carbon fibers, the surrounding matrix is gradually eroded to expose fiber tips, which transform into a needle-like shape with continuous ablation, and the high pressure and flow rates subsequently lead to fiber fracture due to insufficient shear stress resistance. For interfaces — acting as oxidation active sites, ablation initiates at the interfaces between fibers and PyC, bundles and PyC, rods and PyC layers, as well as PyC and PDC, where ablation gaps form to allow gas flow that increases the

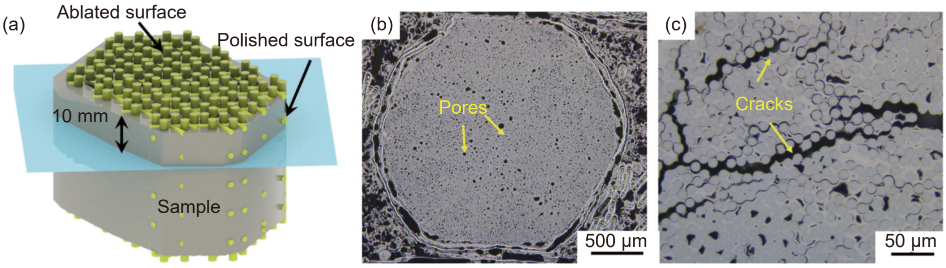

Fig. 13 Internal microstructure of the material after ablation: (a) Observation location of the specimen. (b) Carbon rod. (c) Carbon fiber

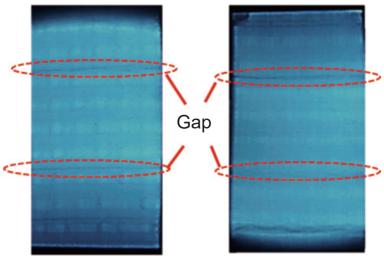

Fig. 14 Real-time X-ray imaging spectra of the post-ablated specimen cross-section

ablation surface area, and the thermal shock caused by temperature fluctuations during pulse intervals further induces delamination and cracks, particularly at these interface regions. As for PyC layers and the matrix, the PyC layers around carbon rods retain their basic contours after ablation, showing excellent ablation resistance, and their "wall" structure effectively protects carbon fibers from severe ablation compared to composites with a single PDC matrix; while the PDC matrix, characterized by weak van der Waals forces, is more prone to ablation and loosening, and the high temperature gradients during heating and cooling cause thermal expansion mismatch, which in turn separates the folded zones within the PDC.

3.4 Ablation behavior analysis of 4D-DM C/C composites under dual-pulse motors

The 4D-DM C/C composites throat component is subjected to mechanical erosion and thermochemical ablation under high temperature and pressure with oxygen. Mechanical erosion entails the granular exfoliation of carbon fibers and the matrix carbon due to gas flow pressure and shear stress, or sheet dentation caused by thermal stress, thermochemical ablation refers to mass loss resulting from reactions with oxidative gases[15]. During SRM firing, various gases are released from propellant combustion. At high temperature and pressure, the C/C composite surface is prone to chemical ablation by oxidizing gases[47]. Studies have shown that H_2O, CO_2 and OH are the primary oxidizing species causing material loss by thermal ablation[15]. The heterogeneous reactions between these gases and the C/C composite surface are as follows:

$$C(s)+H_2O(g)\rightarrow CO(g)+H_2(g) \tag{5}$$

$$C(s)+CO_2(g)\rightarrow 2CO(g) \tag{6}$$

$$C(s)+OH(g)\rightarrow CO(g)+0.5H_2(g) \tag{7}$$

The ablation behavior is governed by the combustion chamber environment, which is dictated by parameters such as temperature, pressure, gas flow velocity, and oxidative gas concentration[48]. These varying conditions lead to distinct ablation mechanisms in different sections of the throat. Furthermore, different parts of the C/C composites also exhibit different ablation behaviors. This study proposes a model to explain the ablation behavior of the 4D-DM C/C composites throat in dual-pulse motors (Fig. 15).

When pulse I is in operation, as the combustion chamber pressure increases, the propellant burning rate rises accordingly, accelerating mass transfer and diffusion processes. This, in turn, promotes Reactions (5–7). Thermochemical ablation dominates this stage, resulting in the formation of conical carbon fibers. The multiple interfaces within the material are preferentially ablated, generating gaps that expand under subsequent gas flow. The PyC layer around the carbon rods thins due to ablation, significantly increasing surface roughness. Upon completion of pulse I, the throat temperature drops rapidly, inducing substantial thermal stresses within the material due to thermal mismatch.

After the pulse interval, when pulse II ignites, the ablation surface temperature of the C/C composites surge due to efficient heat exchange with the high-temperature gas flow. Cyclic thermal shocks at material interfaces exacerbate thermal stresses, leading to further debonding and crack initiation along fiber bundles parallel to the ablation direction. Owing to the higher pressure in pulse II, the C/C composites experiences intensified mechanical erosion and shear forces from the high-velocity flow. Given the low axial shear resistance of carbon fibers, the debonded matrix and individual fibers are readily detached. The combined effects of elevated pressure and gas concentration during pulse II accelerate synergistic mechanical-chemical ablation, resulting in severe surface degradation and rapid fiber recession. Consequently, the average linear ablation rate of pulse II is significantly higher than that of pulse I. The primary ablation mechanism dur-

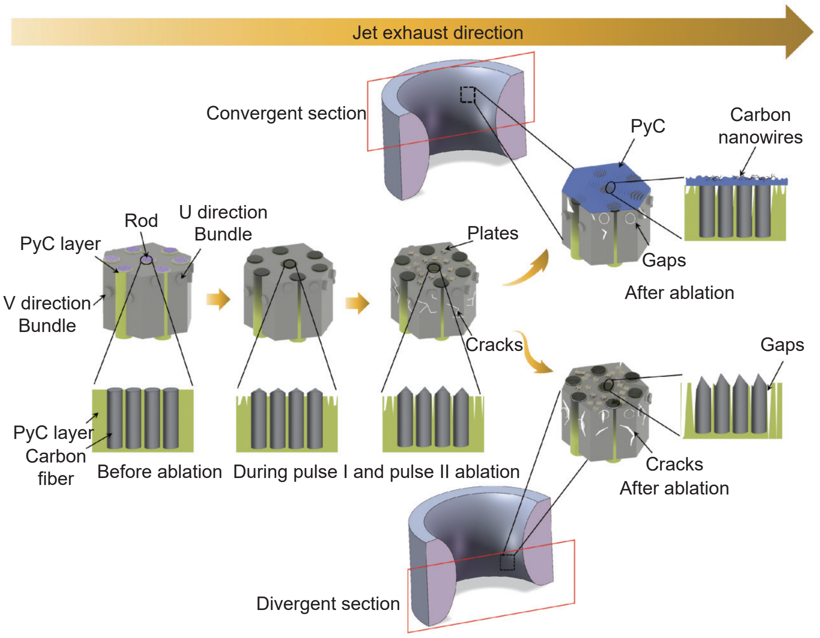

Fig. 15 Schematic diagram of ablation behavior of 4D-DM C/C composites during ablation

ing the pulse I was the oxidation and mechanical scouring of the PyC and PDC matrix, forming a preliminary ablation morphology. In the pulse II, the ablation was markedly intensified, characterized by the propagation of cracks along the interfaces of the multi-layered matrix and the severe layer-by-layer delamination of the PDC, leading to significant structural denudation.

During the post-operation cooling phase, due to the influence of the insulation layer, hydrocarbon gas flows and deposits a layer of PyC and carbon nanowires on the surface of the convergent section, while the thermal expansion mismatch between carbon fibers and the matrix causes differential contraction, widening interfacial gaps in the divergent section. As temperature decreases, these gaps evolve into delamination structures.

4 Conclusion

In this study, 4D DM C/C composites were fabricated using a hybrid woven preform molding process combined with a densification technique integrating CVI and HPIC. The discontinuous ablation behavior of the composites under DPSRM test conditions was investigated. The key findings are summarized as follows:

(1) During preparation of the composites, the carbon rods exhibited a hexagonal cross-section, surrounded by a dense PyC “wall” structure. The linear ablation rates of the composites after pulse I and pulse II were 0.068 and 0.113 mm/s, respectively. Post-test analysis revealed a significant increase in surface roughness. Within the convergent section, PyC deposits and carbon nanowires were observed: the former resulted from the pyrolysis and deposition of the motor’s insulation layer following propellant combustion, while the latter were formed via catalytic reactions involving ferrocene derivatives that migrated from the propellant to the insulation layer and liner during pyrolysis.

(2) In the divergent section, debonding occurred at multiple interfaces, including matrix-fiber, carbon rod-PyC, and within the PDC matrix. This debonding led to crack initiation, which propagated as temperatures decreased, ultimately causing delamination between fiber bundles. The ablation process of the C/C composites under DPSRM conditions is characterized as a discontinuous process involving high-temperature/high-velocity gas erosion, thermochemical ablation by oxygen-containing species and thermal shock.

Declaration of competing interest

The authors declare that they have no known competing financial interests or personal relationships that could have appeared to influence the work reported in this paper.

Acknowledgements

This work was supported by the National Natural Science Foundation of China (52272044, 52125203), the fund of the Shaanxi Laboratory of Advanced Materials (2024ZY-JCYJ-04-05) and the Innovation Foundation for Doctor Dissertation of Northwestern Polytechnical University (CX2025054).

References

[1] Zhang X, Guo L, Liu H, et al. Advanced anti-ablation C/C composites: structural design strategies and future perspective[J]. Materials Today, 2024, 80: 710-736.

[2] Peng L, He G, Li J, et al. Effect of combustion gas mass flow rate on carbon/carbon composite nozzle ablation in a solid rocket motor[J]. Carbon, 2012, 50(4): 1554-1562.

[3] Qiao Y, Liu P, Liu W, et al. Analysis and optimization of flow and heat transfer performance of active thermal protection channel for hypersonic aircraft[J]. Case Studies in Thermal Engineering, 2022, 39: 102476.

[4] Jin X, Fan X, Lu C, et al. Advances in oxidation and ablation resistance of high and ultra-high temperature ceramics modified or coated carbon/carbon composites[J]. Journal of the European Ceramic Society, 2018, 38(1): 1-28.

[5] Zhang M, Liu T, Hu D, et al. Ablation behavior of UHTCs carbide-modified C/C composites in extreme aerobic environments (3000 °C): Evolution mechanisms of oxides film structure[J]. Corrosion Science, 2025, 253: 113036.

[6] Cao Y, Lu J, Zhou Z, et al. Fabrication, mechanical properties and ablation performance of SiCnw/PyC-C/C-HfC-SiC composites with a Si-rich coating via film boiling chemical vapor infiltration and gaseous silicon infiltration[J]. Journal of the European Ceramic Society, 2025, 45(15): 117609.

[7] Schonberg W, Squire M. Predicting high-speed particle impact damage in spacecraft thermal protection systems[J]. Journal of Space Safety Engineering, 2024, 11(1): 87-101.

[8] Natali M, Kenny J M, Torre L. Science and technology of polymeric ablative materials for thermal protection systems and propulsion devices: A review[J]. Progress in Materials Science, 2016, 84: 192-275.

[9] Wang R, Zhang J, Liu B, et al. Ablation of advanced C/C-ZrC-SiC leading edge composites[J]. Corrosion Science, 2024, 226: 111648.

[10] Li K, Jing X, Fu Q, et al. Effects of porous C/C density on the densification behavior and ablation property of C/C–ZrC–SiC composites[J]. Carbon, 2013, 57: 161-168.

[11] Yang J, Ge J, Jing Z, et al. Analysis of thermochemical ablation and mechanical erosion of C/C composites based on macro-meso-scale numerical simulation methods[J]. International Journal of Heat and Mass Transfer, 2024, 228: 125658.

[12] Zha B, Su Q, Shi Y, et al. Study on plasma ablation behavior of C/C composite materials under particle erosion[J]. IOP Conference Series: Materials Science and Engineering, 2018, 423.

[13] Liu X, Fu Q, Wang H, et al. Microstructure, thermophysical property and ablation behavior of high thermal conductivity carbon/carbon composites after heat-treatment[J]. Chinese Journal of Aeronautics, 2020, 33(5): 1541-1548.

[14] Qin F, Peng L, Li J, et al. Numerical simulations of multiscale ablation of Carbon/Carbon throat with morphology effects[J]. AIAA Journal, 2017, 55(10): 3476-3485.

[15] Li S, Zhang B, Meng S, et al. Ablation behavior of carbon-carbon composite nozzles produced by different carbon fibers in a small solid rocket motor[J]. Aerospace Science and Technology, 2025, 159: 109985.

[16] Wang L, Tian W, Chen L, et al. Investigation of carbon–carbon nozzle throat erosion in a solid rocket motor under acceleration conditions[J]. International Journal of Aeronautical and Space Sciences, 2020, 22(1): 42-51.

[17] Wen Z, Zhang R, Hou C, et al. A PD-FEM coupling approach for the analysis of oxidation and out-of-plane compression failure of 2D braided C/C composites[J]. Engineering Fracture Mechanics, 2025, 316: 110866.

[18] Wang K, Xu C, Gao B, et al. Damage evolution and failure behavior of 3D needled Carbon/Carbon composites under compressive at ultra-high temperatures up to 2800 °C[J]. Journal of the European Ceramic Society, 2025, 45(6): 117183.

[19] Cheng Y, Lyu Y, Xie Y, et al. Starting from essence to reveal the ablation behavior and mechanism of 3D PyC C_f/ZrC-SiC composite[J]. Corrosion Science, 2022, 201(201): 110261.

[20] Shi Y A, Zha B L, Sun Z S, et al. Air plasma ablation/erosion test for 4D C/C composites used in the throat of solid rocket motor[J]. Ceram Int, 2022, 48(11): 15582-15593.

[21] Farhan S, Ul-Haq N, Kuo W S. Degradation behavior of 4D carbon/carbon composites under supersonic oxidative air plasma[J]. Ceramics International, 2013, 39(6): 7135-7142.

[22] Vignoles G L, Aspa Y, Quintard M. Modelling of carbon–carbon composite ablation in rocket nozzles[J]. Composites Science and Technology, 2010, 70(9): 1303-1311.

[23] Zahid M, Sharma R. Thermal shock resistance of 4D-inplane carbon/carbon composite based on micro-structurally informed effective properties[J]. Materials Today Communications, 2020, 25: 101637.

[24] Wang R, Cheng C, Yang X, et al. Ablation behavior of C/C-ZrC-SiC composites under oxyacetylene, plasma, and plasma-solid particle environments: a comparative investigation[J]. Materials Characterization, 2025, 219: 114649.

[25] Zhang S, Zhang J, Hu S, et al. Ablation behavior and mechanism of $MoSi_2$/mica/HSM modified CF/BPR composites during prolonged ablation of oxyacetylene flame[J]. Ceramics International, 2025.

[26] Zhang J, Su X, Li X, et al. Ablation behaviour and mechanical performance of ZrB_2-ZrC-SiC modified carbon/carbon composites prepared by vacuum infiltration combined with reactive melt infiltration[J]. New Carbon Materials, 2024, 39(4): 633-644.

[27] Wang L, Tian W, Guo Y, et al. Effects of CVD carbon on the erosion behavior of 5D carbon-carbon composite in a solid rocket motor[J]. Applied Composite Materials, 2020, 27(4): 391-405.

[28] Zhao J, Li K, Li H, et al. The influence of thermal gradient on pyrocarbon deposition in carbon/carbon composites during the CVI process[J]. Carbon, 2006, 44(4): 786-791.

[29] Li B, Huang D, Li T, et al. The positive role of mesophase-pitch-based carbon fibers in enhancing thermal response behavior in Carbon/Carbon composites[J]. Materials Characterization, 2023, 196: 112630.

[30] Kumar S, Kushwaha J, Mondal S, et al. Fabrication and ablation testing of 4D C/C composite at 10MW/m^2 heat flux under a plasma arc heater[J]. Materials Science and Engineering: A, 2013, 566: 102-111.

[31] Zaman W, Li K, Ikram S, et al. Residual compressive and thermophysical properties of 4D carbon/carbon composites after repeated ablation under oxyacetylene flame of 3000 °C[J]. Transactions of Nonferrous Metals Society of China, 2013, 23(6): 1661-1667.

[32] Zha B, Shi Y, Wang J, et al. Effects of oxygen content on the ablation/erosion behavior of 4D carbon/carbon composite material[J]. Materials Research Express, 2020, 7(8): 085601.

[33] Liu Y, Li X, Zhu P, et al. Ablation characteristics of insulator under high-temperature gas dual-pulse erosion[J]. Defence Technology, 2022, 18(10): 1875-1885.

[34] Li Y, Chen X, Xu J, et al. Three-dimensional multi-physics coupled simulation of ignition transient in a dual pulse solid rocket motor[J]. Acta Astronautica, 2018, 146: 46-65.

[35] Lee Y J, Joo H J. Investigation on ablation behavior of CFRC composites prepared at different pressure[J]. Composites Part A: Applied Science and Manufacturing, 2004, 35(11): 1285-1290.

[36] Liu Y, Xia Z, Ma L, et al. Microstructure and ablation mechanism of C/C-ZrC-SiC composite in the solid scramjet plumes environment[J]. Materials Characterization, 2023, 198: 112754.

[37] Natali M, Puri I, Rallini M, et al. Ablation modeling of state of the art EPDM based elastomeric heat shielding materials for solid rocket motors[J]. Computational Materials Science, 2016, 111: 460-480.

[38] Jia X, Li G, Sui G, et al. Effects of pretreated polysulfonamide pulp on the ablation behavior of EPDM composites[J]. Materials Chemistry and Physics, 2008, 112(3): 823-830.

[39] Valdebenito C, Gaete J, Osorio C, et al. Evaluation of mono and bimetallic ferrocene-based 1, 2, 3-triazolyl compounds as burning rate catalysts for solid rocket motor[J]. ACS Omega, 2023, 8(38): 35242-35255.

[40] Selvakumar S, Rao G S, Reddy K A. Diffusion of labile chemical species in HTPB and HTPB-XT solid propellants and its effect over solid rocket motor properties on aging-A study[J]. Propellants Explosives Pyrotechnics, 2021, 46(5): 782-790.

[41] Leonhardt A, Hampel S, Müller C, et al. Synthesis, properties, and applications of ferromagnetic-filled carbon nanotubes[J]. 2006, 12(6): 380-387.

[42] Guo H, Huo D, Zhao H, et al. Synthesis, anti-migration and catalytic effect of ferrocene azine derivatives on the thermal decomposition of ammonia perchlorate[J]. Zeitschrift Fur Anorganische Und Allgemeine Chemie, 2022, 648(8).

[43] Barreiro A, Hampel S, Rümmeli M H, et al. Thermal decomposition of ferrocene as a method for production of single-walled carbon nanotubes without additional carbon sources[J]. The Journal of Physical Chemistry B, 2006, 110(42): 20973-20977.

[44] Kuwana K, Saito K. Modeling ferrocene reactions and iron nanoparticle formation: Application to CVD synthesis of carbon nanotubes[J]. Proceedings of the Combustion Institute, 2007, 31: 1857-1864.

[45] Dilsiz N, Ünver A. Characterization studies on aging properties of acetyl ferrocene containing HTPB-based elastomers[J]. Journal of Applied Polymer Science, 2006, 101(4): 2538-2545.

[46] Hui W H, Bao F T, Wei X G, et al. Ablation performance of a 4D-braided C/C composite in a parameter-variable channel of a Laval nozzle in a solid rocket motor[J]. New Carbon Materials, 2017, 32(4): 365-373.

[47] Jiang X, Tian H, Tan G, et al. Experiments of ablation characteristics for different nozzle materials and transient simulations on thermochemical erosion in hybrid rocket motors[J]. Acta Astronautica, 2023, 212: 455-466.

[48] Yin J, Zhang H B, Xiong X, et al. Ablation performance of Carbon/Carbon composite throat after a solid rocket motor ground ignition test[J]. Applied Composite Materials, 2011, 19(3-4): 237-245.